JOC The Journal of Organic Chemistry
Article
pubs.acs.org/joc

A Computational Study of the Copper(II)-Catalyzed Enantioselective Intramolecular Aminooxygenation of Alkenes

Lee Belding,[†] Sherry R. Chemler,[‡] and Travis Dudding*,[†]

[†]Department of Chemistry, Brock University, St. Catharines, Ontario, Canada L2S 3A1
[‡]Department of Chemistry, The State University of New York at Buffalo, Buffalo, New York 14260, United States

Supporting Information

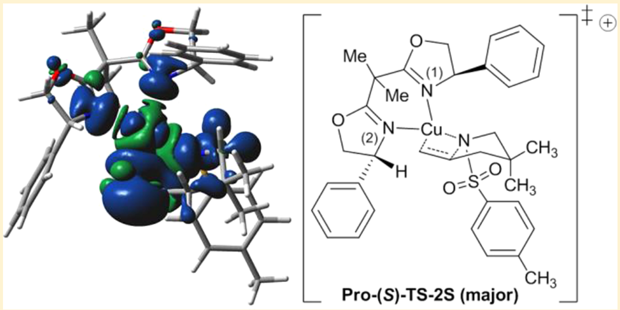

ABSTRACT: The origin of the enantioselectivity in the [Cu(*R*,*R*)-Ph-box](OTf)$_2$-catalyzed intramolecular aminooxygenation of *N*-sulfonyl-2-allylanilines and 4-pentenylsulfonamides to afford chiral indolines and pyrrolidines, respectively, was investigated using density functional theory (DFT) calculations. The pyrrolidine-forming transition-state model for the major enantiomer involves a chairlike seven-membered cyclization transition state with a distorted square-planar copper center, while the transition-state model for the minor enantiomer was found to have a boatlike cyclization geometry having a distorted tetrahedral geometry about the copper center. Similar copper-geometry trends were observed in the chiral indoline-forming reactions. These models were found to be qualitatively consistent with experimental results and allow for rationalization of how substitution on the substrate backbone and *N*-sulfonyl substituent affect the level of enantioselectivity in these and related copper(II)-catalyzed enantioselective reactions.

■ INTRODUCTION

The development of catalytic enantioselective alkene difunctionalization reactions is an important and burgeoning area of chemical research.[1−5] Powerful transformations such as alkene dihydroxylation[3] and alkene aminohydroxylation,[5] for example, enable the concise enantioselective synthesis of valuable chiral intermediates for use in fine chemical and natural product synthesis. Transition-metal catalysis has played a prominent role in the development of enantioselective alkene difunctionalization reactions.[1−5] Over the past several years, enantioselective alkene difunctionalization reactions catalyzed by copper(II) 2,2′-isopropylidenebis[(4*R*)-4-phenyl-2-oxazoline] ditriflate {[Cu(*R*,*R*)-Ph-box](OTf)$_2$} and copper(II) 2,2′-isopropylidenebis[(4*R*,5*S*)-4,5-diphenyl-2-oxazoline] ditriflate {[Cu(4*R*,5*S*)-di-Ph-box](OTf)$_2$,} have been reported.[6−14] These chiral copper catalysts are well-known in the area of asymmetric catalysis,[15,16] and their attributes include their generally robust nature and well-defined composition.[17] Despite their wide availability, their use as catalysts in the enantioselective difunctionalization of alkenes is a relatively recent development. Many of the reported copper-catalyzed alkene difunctionalization reactions involve the cyclization of a sulfonamide nitrogen onto a pendant alkene (usually terminal) to form a new stereocenter with good to excellent enantiomeric excess.[6−13] These reactions include the aminooxygenation, carboamination, aminohalogenation, and hydroamination of alkenes.[6−13] Some of these reactions are summarized in eqs 1−5. It is noteworthy that in these examples the reaction conditions (type of reaction), the backbone substituents of the substrate, and the *N*-sulfonyl substituent all can affect the level of enantioselectivity. Although a detailed transition-state model, supported by DFT calculations, has been proposed to rationalize the diastereoselectivity obtained in the copper(II) carboxylate-promoted aminooxygenation reactions of α-substituted-γ-pentenylsulfonamides,[18−20] still lacking is a well-developed understanding of the origin of the enantioselectivity in the [Cu(*R*,*R*)-Ph-box](OTf)$_2$-catalyzed aminooxygenation reaction set reported recently by Chemler et al.[18−20] and summarized in eqs 1 and 2. The development of a rigorous understanding of the enantioselectivity origin in the aminooxygenation reaction could more broadly impact the development of copper-catalyzed alkene difunctionalization reactions, as the enantioselective carboamination, aminohalogenation, and hydroamination reactions summarized in eqs 3−5, for example, are thought to occur via the same enantiodetermining aminocupration transition state (vide infra).

Catalytic Enantioselective Aminooxygenation. Recently we reported strong spectroscopic and kinetic evidence as well as DFT calculations suggesting that *cis*-aminocupration is the rate-determining step in the copper(II) carboxylate-*promoted* intramolecular alkene aminooxygenation reaction (eq 6).[18−20] With H/D-substituted alkenes, an inverse secondary kinetic isotope effect was observed in the alkene addition step (eq 6), providing further support that it is the rate-determining step. The reaction kinetics of the enantioselective copper-

Received: July 30, 2013
Published: September 13, 2013

dx.doi.org/10.1021/jo401665n | *J. Org. Chem.* 2013, 78, 10288−10297

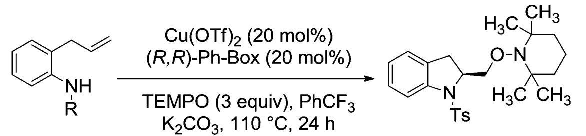

(1)

1a, R = Ts
1b, R = Ms

2a, 88% yield, 87% ee
2b, 50% yield, 63% ee

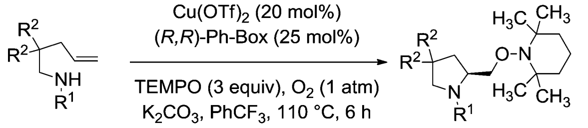

(2)

3a, R^1 = Ts, R^2 = Me
3b, R^1 = 3,5-di-*t*-BuC$_6$H$_3$, R^2 = Me

4a, 88% yield, 88% ee
4b, 92% yield, 96% ee

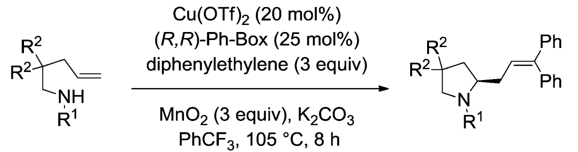

(3)

3a, R^1 = Ts, R^2 = Me
3c, R^1 = Ms, R^2 = Me
3d, R^1 = Ts, R^2 = H

5a, 74% yield, 92% ee
5b, 88% yield, 55% ee
5c, 62% yield, 80% ee

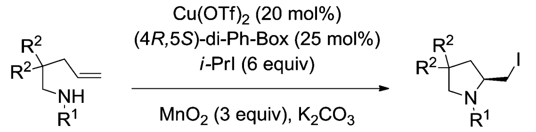

(4)

3a, R^1 = Ts, R^2 = Me
3d, R^1 = Ts, R^2 = H
3e, R^1 = 3,5-di-*t*-BuC$_6$H$_3$, R^2 = H

6a, 81% yield, 88% ee
6b, 77% yield, 73% ee
6d, 85% yield, 88% ee

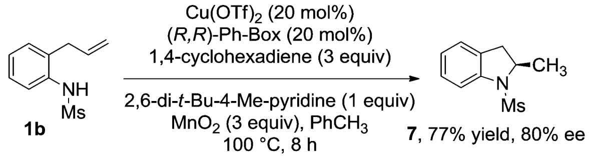

(5)

1b

7, 77% yield, 80% ee

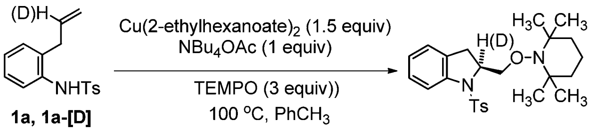

(6)

1a, 1a-[D]

k_H/k_D = 0.90 ± 0.03

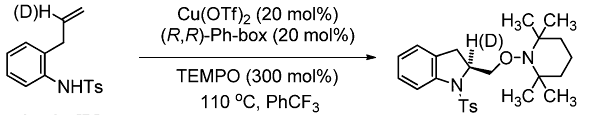

(7)

1a, 1a-[D]

k_H/k_D = 0.90 ± 0.04

catalyzed aminooxygenation reaction (eq 1) was also recently examined,[21] and the reaction was found to be first order in sulfonamide **1a**, first order in [Cu(*R*,*R*)-Ph-box](OTf)$_2$, and zeroth order in (2,2,6,6-tetramethylpiperidin-1-yl)oxyl (TEMPO). Additionally, with H/D-substituted alkenes, an inverse secondary kinetic isotope effect was observed in the alkene addition step (eq 7), indicating that it is also the rate-determining step in the catalytic reaction.

On the basis of the similarity of the copper-catalyzed and copper-promoted reactions, including their similar diastereoselectivity trends,[18−20] we envisioned the proposed catalytic aminooxygenation reaction mechanism shown in Scheme 1. In this reaction, association of the amine nucleophile with the copper(II) center to form **8a** or **8b** is thought to be rapid, and this step is followed by rate-determining *cis*-aminocupration through a cyclic pro-(*S*) transition state (**TS-1S**). Loss of H$^+$ from the sulfonamide likely occurs after [Cu] association, when its pK_a would be lower. A base such as K$_2$CO$_3$ is usually necessary to sequester this proton (eqs 1−5), but additional base was not necessary for the aminooxygenation reaction of **1a**. It is likely that TEMPO anion (TEMPO is used in excess) serves as the base in this reaction. The resulting organocopper(II) intermediate **9a** or **9b** is unstable and undergoes C−Cu(II) bond homolysis to give Cu(I) and carbon radical **10**, followed by direct trapping of the carbon radical with TEMPO radical to provide the aminooxygenation product.[21] Reversible coordination of the triflate counterion for intermediates **8** and **9** reflects a mechanism refinement based upon the results of the calculations presented herein (vide infra). While Chemler and co-workers have proposed a working mechanistic hypothesis to rationalize the formation of the major enantiomer [e.g., pro-(*S*) **TS-1S**; Scheme 1],[7,21] no proposal for the competing pro-(*R*) transition state has been put forth. We report herein a detailed DFT study providing energy-minimized models of the competing pro-(*S*) and pro-(*R*) transition states that shed light on the underlying factors that control this reaction's absolute stereochemistry.

■ METHODS

Calculations were carried out at the Kohn−Sham hybrid-DFT UB3LYP[22,23] level of theory using the Gaussian 09[24] and GaussView version 5.0.8 programs. The GenECP method was employed with a 6-31G(d) basis set applied to all atoms except copper (i.e., H, C, N, O, F, and S); copper was computed using the Los Alamos LAN2DZ[25−28] basis set, as in our theoretical study of the copper-promoted aminooxygenation reaction.[18] To account for the experimental use of polar solvents in this system, the integral equation formalism polarized continuum solvation model (IEFPCM)[29] was used throughout the computations. Because the Gaussian 09 program does not contain default solvent parameters for the reaction solvent trifluorotoluene (ε = 9.18), those of 1,2-dichloroethane (ε = 10.13), which is supported by the program and has a similar dielectric constant, were used instead.[30] The calculations were run at 383.15 K (110 °C) for consistency with experimental protocols. All of the transition states were confirmed to have only one imaginary frequency, and the intrinsic reaction coordinate (IRC) method[31] was used with default parameters followed by a geometry optimization to confirm the product species (minima, containing only real frequencies) resulting from the path of steepest descent for each transition state. To further support the computational data, single-point energies were computed using the ωB97XD[32] functional in place of B3LYP for better representation of long-range dispersion interactions, as well as at the ωB97XD/6-311G+(d,p)/SCRF=dichloroethane level of theory. Because of the elevated temperatures at which the experiments were conducted, thermal energy corrections obtained from the optimized structures were included in all of the single-point energies. These data can be found in the Supporting Information. Natural bond order (NBO) analysis was performed using Gaussian NBO version 3.1.[33] The term "tetrahedral twist angle" (θ_{TTA}) is defined as the angle between the plane containing the two nitrogen atoms of the bis(oxazoline) ligand [$N_{lig(1)}$ and $N_{lig(2)}$] and the copper atom and the plane containing of the sulfonamide nitrogen (N_{sub}), the terminal carbon of the substrate's olefin (C_{sub1}), and the copper atom. To compute θ_{TTA}, the Mercury 2.4 program[34] was used.

The reported ground states (e.g., Figures 1 and 2) were located using molecular-mechanics-based conformational distribution searches (MMFF94), which were performed using Spartan '04.[35] In one conformational distribution search, the coordinates of the copper atom, $N_{lig(1)}$, and $N_{lig(2)}$ were constrained. In another conformational distribution search, N_{sub} was also constrained. The five lowest-energy conformers from each distribution search with observably different

Scheme 1. Proposed Copper-Catalyzed Enantioselective Aminooxygenation Cycle

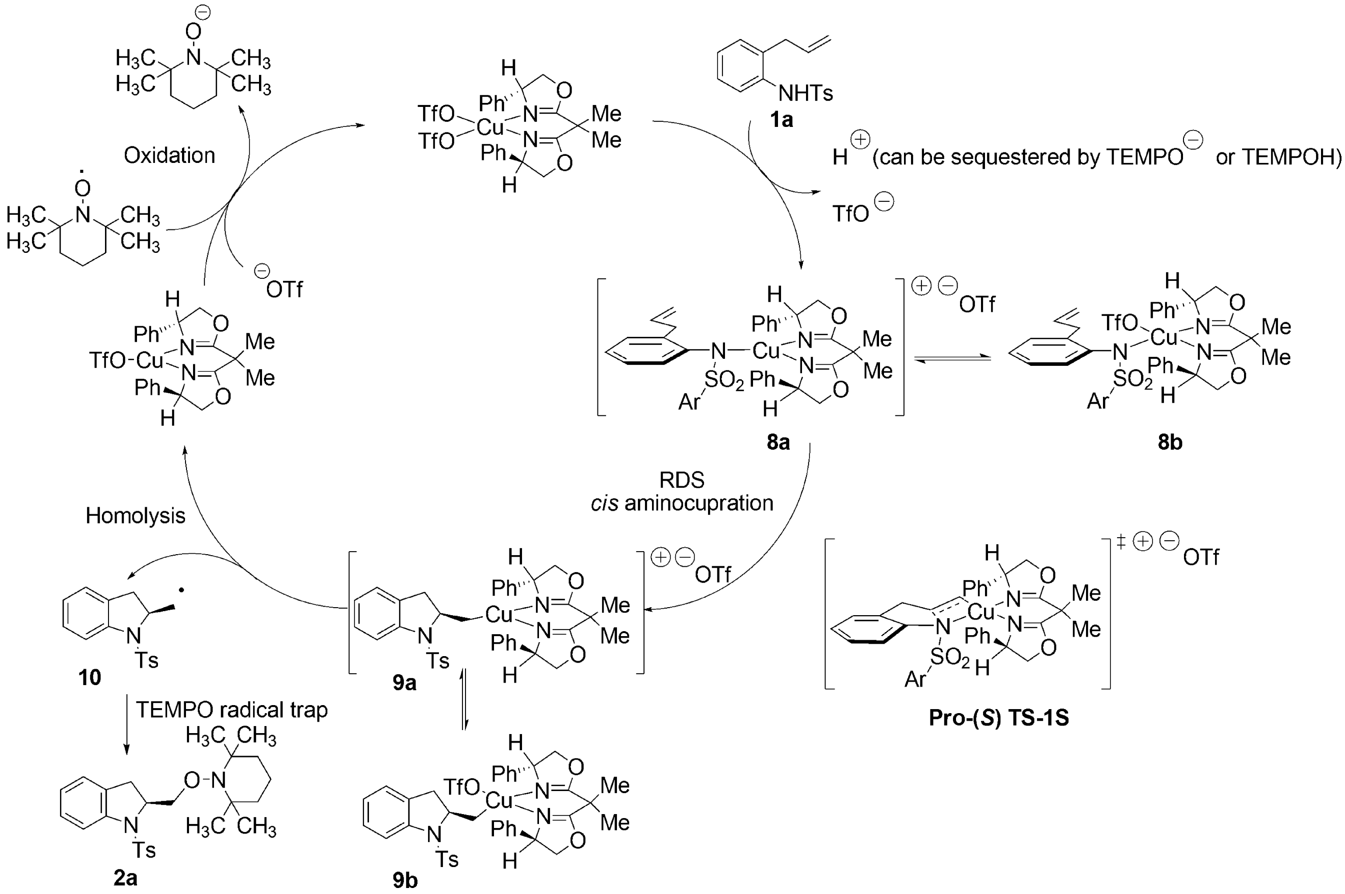

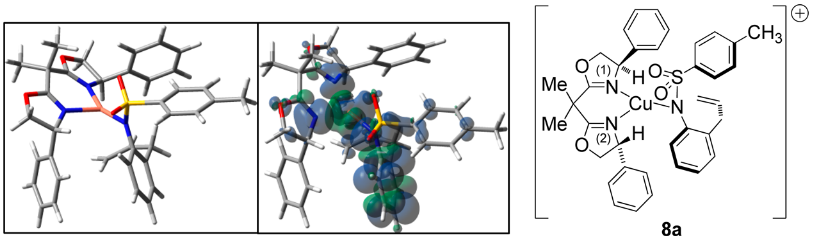

Figure 1. Calculated ground-state complex [Cu(*R*,*R*)-Ph-Box(*N*-tosyl-*o*-allyl anilide)]$^{1+}$ (**8a**) resulting from coordination of sulfonamide **1a** to[Cu(*R*,*R*)-Ph-box](OTf)$_2$. Spin densities: Cu (50.8%), N$_{\mathrm{sub}}$ (22.4%), N$_{\mathrm{lig(1)}}$ (8.8%), N$_{\mathrm{lig(2)}}$ (4.8%), Ar$_{\mathrm{sub}}$ 10.9%. Bond distances: O$_{\mathrm{sulfonyl}}$−Cu (2.84 Å), N$_{\mathrm{sub}}$−Cu (1.95 Å), N$_{\mathrm{lig(1)}}$−Cu (2.02 Å), N$_{\mathrm{lig(2)}}$−Cu (2.05 Å). Mulliken charges: N$_{\mathrm{lig(1)}}$ (−0.514), N$_{\mathrm{lig(2)}}$ (−0.503), Cu (0.602), N$_{\mathrm{sub}}$ (−0.795), C$_{\mathrm{sub1}}$ (−0.369), C$_{\mathrm{sub2}}$ (−0.066), S (1.328).

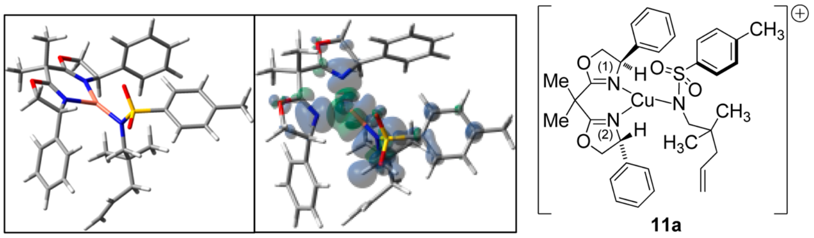

Figure 2. Calculated ground-state complex [Cu(*R*,*R*)-Ph-Box(*N*-tosyl-2,2-dimethylpent-4-en-1-amide)]$^{1+}$ (**11a**) resulting from coordination of sulfonamide **3a** to [Cu(*R*,*R*)-Ph-box](OTf)$_2$. Spin densities: Cu (49.1%), N$_{\mathrm{lig(1)}}$ (5.1%), N$_{\mathrm{lig(2)}}$ (8.2%), N$_{\mathrm{sub}}$ (32.2%). Bond distances: O$_{\mathrm{sulfonyl}}$−Cu (2.83 Å), N$_{\mathrm{sub}}$−Cu (1.91 Å), N$_{\mathrm{lig(1)}}$−Cu (2.00 Å), N$_{\mathrm{lig(2)}}$−Cu (2.02 Å). Mulliken charges: N$_{\mathrm{lig(1)}}$ (−0.522), N$_{\mathrm{lig(2)}}$ (−0.521), Cu (0.604), N$_{\mathrm{sub}}$ (−0.695), C$_{\mathrm{sub1}}$ (−0.387), C$_{\mathrm{sub2}}$ (−0.070), S (1.310).

geometries were then reoptimized using Gaussian 09 at the above-mentioned level of theory. The lowest-energy minimum obtained from this procedure was chosen as the best approximation to the ground-state complex.

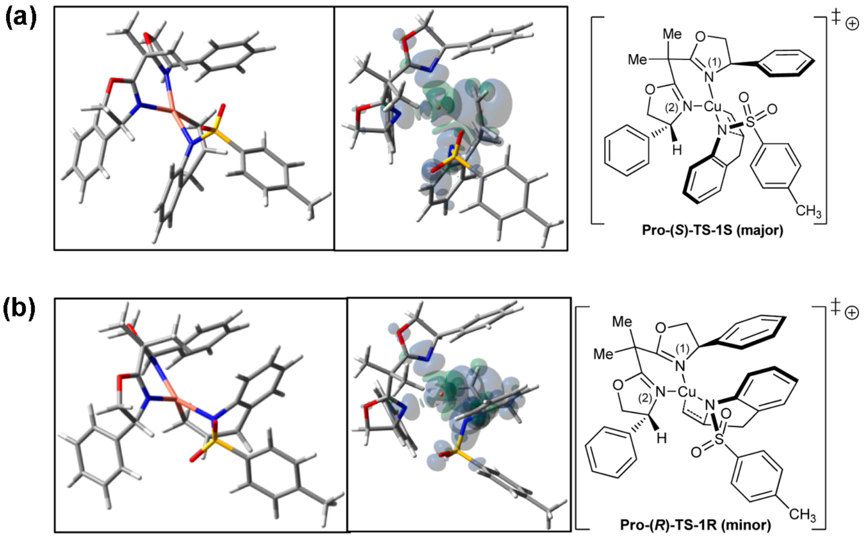

Figure 3. (a) Computed *N*-tosyl-*o*-allyl aniline pro-(*S*) $(N{-}C)_{sub}$ bond-forming transition-state structure (**TS-1S**). Mulliken charges: $N_{lig(1)}$ (−0.468), $N_{lig(2)}$ (−0.475), Cu (0.429), N_{sub} (−0.757), C_{sub1} (−0.476), C_{sub2} (0.051), S (1.307). Spin densities: Cu (43.3%), N_{sub} (15.6%), C_{sub1} (26.8%), $N_{lig(1)}$ and $N_{lig(2)}$ (9.7%). (b) Computed *N*-tosyl-*o*-allyl aniline pro-(*R*) $(N{-}C)_{sub}$ bond-forming transition-state structure (**TS-1R**). Mulliken charges: $N_{lig(1)}$ (−0.476), $N_{lig(2)}$ (−0.461), Cu (0.431), N_{sub} (−0.780), C_{sub1} (−0.466), C_{sub2} (0.051), S (1.302). Spin densities: Cu (43.1%), N_{sub} (15.8%), C_{sub1} (27.3%), $N_{lig(1)}$ and $N_{lig(2)}$ (7.7%).

RESULTS AND DISCUSSION

Ground-State Analysis. At the outset of this study, we investigated the two ground-state species resulting from coordination of [Cu(*R*,*R*)-Ph-box]$(OTf)_2$ to *N*-tosyl-*o*-allyl aniline (**1a**) and *N*-tosyl-2,2-dimethylpent-4-en-1-amine (**3a**). While some copper(II) complexes are known to exhibit six-coordinate octahedral geometries,[36] copper(II) complexes with bis(oxazoline) ligands preferentially form four-coordinate square planar and five-coordinate square-pyramidal species.[15,16,37] Interestingly, however, our calculations revealed the most favorable substrate−catalyst ground-state complex, $[Cu(R,R)\text{-Ph-Box}(N\text{-tosyl-}o\text{-allyl anilide})]^{1+}$ (**8a**), to be a three-coordinate species (Scheme 1 and Figure 1). Steric crowding around copper resulting from coordination of the substrate and ligand prevents the formation of a four-coordinate species that would result from further ligation of a sulfonamide oxygen atom, as seen with similar substrates in the presence of less sterically demanding copper complexes.[18] Moreover, this steric crowding prevents the direct ligation of $^{-}$OTf, and the triflate acts only as a counterion, residing outside the direct coordination sphere of the copper center. Consequently, to simplify our calculations, the triflate counterion was omitted, and thus, the modeled complexes had an overall +1 charge.

The copper center of the ground state of $[Cu(R,R)\text{-Ph-Box}(N\text{-tosyl-}o\text{-allyl anilide})]^{1+}$ (**8a**) possesses a distorted trigonal-planar geometry. Making up the trigonal plane are the copper, $N_{lig(1)}$, $N_{lig(2)}$, and N_{sub} atoms. The sulfonamide oxygen resides above the trigonal plane at a distance of 2.84 Å from the copper atom in an apical position. NBO analysis revealed a correlation between the three N−Cu bond distances and their corresponding $N_{(LP)} \rightarrow Cu_{(LP*)}$ donor−acceptor stabilization energies. Specifically, $N_{lig(1)}$ and $N_{lig(2)}$ show donor−acceptor energies (E_{NBO}) of 10.85 and 14.56 kcal/mol and have N−Cu bond distances of 2.05 and 2.02 Å, respectively, while the N_{sub}−Cu bond has a length of 1.95 Å with an E_{NBO} of 24.73 kcal/mol. Because Cu(II) has an unpaired electron, spin density analyses were performed in order to determine how the SOMO is distributed over the complex. It was found that 86.8% of the SOMO resides on Cu and the three nitrogen atoms, with 22.4% on N_{sub}, 10.9% on the aniline ring, and 50.8% on copper.

The structure of $[Cu(R,R)\text{-Ph-Box}(N\text{-tosyl-2,2-dimethylpent-4-en-1-amide})]^{1+}$ (**11a**) (Figure 2) shares many similarities with that of **8a**. In particular, the copper geometry in **11a** is also distorted trigonal-planar, and a similar relationship between the three N−Cu bond distances and their corresponding $N_{(LP)} \rightarrow Cu_{(LP*)}$ donor−acceptor stabilization energies was observed. Specifically, the $N_{lig(1)}$−Cu and $N_{lig(2)}$−Cu bond distances are 2.02 and 2.00 Å with NBO donor−acceptor energies of 14.15 and 17.01 kcal/mol, respectively, while the N_{sub}−Cu distance is 1.91 Å with an E_{NBO} of 24.73 kcal/mol. Furthermore, the sulfonamide oxygen of **11a** occupies an apical coordination site with respect to the copper atom at a distance of 2.83 Å with an E_{NBO} of 3.04 kcal/mol, consistent with the results for **8a**, but in contrast to ground state **8a**, the lack of an aniline ring system in **11a** results in delocalization of the SOMO almost entirely onto Cu and the three N atoms (94%), with 30% of the spin density on N_{sub} and 49% on copper.

Transition State Analysis. From ground state **8a**, the lowest-energy pro-(*S*) and pro-(*R*) transition states for the *N*-tosyl-*o*-allyl aniline substrate **1a** (**TS-1S** and **TS-1R**, respectively) were calculated (Figure 3). The pro-(*S*) mode of addition via **TS-1S** was favored by $\Delta\Delta G^{\ddagger}$ = 1.5 kcal/mol (calculated ee = 75%), which is qualitatively consistent with the experimental observations (eq 1; vide supra). A notable feature of these two transition states is how the coordination geometry of copper differs for the two stereofacial modes of addition. **TS-1S** has a tetrahedral twist angle (θ_{TTA}) of 26.25° and thus a distorted square-planar geometry, while **TS-1R** has a θ_{TTA} of 50.45° and hence a distorted tetrahedral geometry.[38] Spin density analysis of **TS-1S** revealed a spin density of 26.8% on C_{sub1} accompanied by a 7.5% decrease in spin density on Cu and a 6.8% decrease in spin on N_{sub} relative to ground state **8a**. Since the majority of the spin still resides on Cu, it is likely that the SOMO is simply delocalized onto the coordinated atoms, while the $(N{-}C)_{sub}$ bond formation itself possesses a noticeable level of charge separation, as supported by the change in Mulliken charges on going from the ground state to **TS-1S** [Mulliken charges: N_{sub} (−0.795), C_{sub1} (−0.369) for **8a**; N_{sub} (−0.757), C_{sub1} (−0.467) for **TS-1S**].

Placed in the context of the steric environment created by the C_2-symmetric nature of the metal−ligand complex and the simple depiction of stereoinduction in Figure 4b, the N substituent is confined to two of the four existing quadrants. The specific quadrants to which the N substituent is confined differ for the two stereofacial modes of addition. For the case at hand, it is observed that in the pro-(*R*) mode of addition the N substituent can reside only in quadrant QII or QIII, while in the pro-(*S*) addition mode the N substituent lies in quadrant QI or QIV. Thus, the pro-(*R*) transition states, as opposed to the pro-(*S*) transition states, suffer from more unfavorable van der Waals contacts between the N substituent and the phenyl group of the Ph-box ligand.

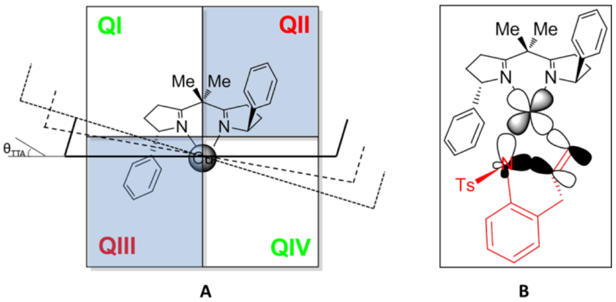

Figure 4. (a) Graphic representation the tetrahedral twist angle (θ_{TTA}) and the quadrant model of steric induction. (b) Pictorial representation of the orbital alignment for $(N-C)_{sub}$ bond formation in **TS-1S**.

Entailed with this picture is the concept of the tetrahedral twist metric θ_{TTA}, which as noted above is the distortion from an ideal planar geometry about copper. As can be seen from this model, to alleviate repulsive steric contacts, the pro-(*R*) series of transition states adopt a larger θ_{TTA}, resulting in poorer orbital overlap and an increase in $\Delta\Delta G^{\ddagger}$, rendering the reaction selective for pro-(*S*). It thus appears that optimal orbital alignment in this system occurs when the copper's 3d orbitals are coplanar with the π-bond of the olefin and the lone pairs of N_{sub} (Figure 4a). This is evidenced by the resulting differences in NBO stabilization energies, bond distances, and overall free energies of activation (summarized in Table 1; vide infra). However, the large 3d orbitals of Cu can tolerate significant deviation from planarity.

We next examined the aminocupration of *N*-tosyl-2,2-dimethylpent-4-en-1-amine (**3a**) (eq 2; vide supra), for which the lowest-energy pro-(*S*) and pro-(*R*) transition states (**TS-2S** and **TS-2R**, respectively) are shown in Figure 5. Again, a difference in coordination geometry is observed for the two stereofacial transition states (**TS-2S**, θ_{TTA} = 13.38°; **TS-2R**, θ_{TTA} = 44.21°), rendering **TS-2S** lower in free energy by $\Delta\Delta G^{\ddagger}$ = 2.7 kcal/mol, corresponding to a calculated ee of 93.4%. However, in this aliphatic substrate, there is an interesting trend not applicable to the aromatic substrate wherein the substrate adopts a seven-membered-ring-type chair or boat conformation depending on the stereofacial mode of addition.[39,40] Specifically, **TS-2S** takes on a chair conformation, while **TS-2R** takes on a boat conformation. The reason for this can be rationalized within the context of the quadrant model. In **TS-2S**, the tosyl group sits in an empty quadrant, while in **TS-2R**, it lies in an occupied quadrant, generating unfavorable van der Waals contacts with the phenyl group of the Ph-box ligand. When the substrate backbone takes on a chair conformation, the geminal dimethyl unit forces the tosyl group further into this unfavorable quadrant, magnifying the steric effect. Thus, the substrate adopts a boat-type transition state to help alleviate steric repulsion.

The NBO energies and bond-forming and bond-breaking distances for competing transition states **TS-1S** and **TS-1R** as well as those for **TS-2S** and **TS-2R** are summarized in Table 1. Comparison of the NBO energies indicates that the distorted square-planar geometries provide greater stabilization (Table 1). In the *N*-tosyl-*o*-allyl aniline series, donation of the alkene double bond ($C_{sub1}{=}C_{sub2}$) to copper is 2.96 kcal/mol greater in **TS-1S** than in **TS-1R**. Additionally, lone-pair donation of N_{sub} to the alkene double bond is 5.04 kcal/mol greater in **TS-1S** than in **TS-1R**. As a result, **TS-1S** has a shorter $(N-C)_{sub}$ bond-forming distance, a shorter $C_{sub1}-Cu$ interatomic distance, and a longer $N_{sub}-Cu$ distance. Taken together, these bond distances and corresponding NBO donor−acceptor energies suggest that $(N-C)_{sub}$ and $C_{sub1}-Cu$ bond making and $N_{sub}-Cu$ bond breaking are more developed in **TS-1S** than in **TS-1R**. This is further exemplified by the lower Mulliken charge on N_{sub} (**TS-1S** = −0.757, **TS-1R** = −0.780) and the higher charge on the terminal CH_2 carbon of the olefin (**TS-1S** = −0.476, **TS-1R** = −0.466) (Figure 3), signifying that in **TS-1S** the negative charge on nitrogen is being donated to the olefin to a larger extent. Analysis of the spin density within **TS-2S** revealed the presence of 24.7% of the spin density on C_{sub1} accompanied by a 6.0% decrease in spin density on Cu and a 15.8% decrease in spin density on N_{sub} relative to ground state **11a**. Similar to **TS-1S**, the bulk of the spin density still resides on Cu, with the SOMO delocalized onto the coordinated atoms. Moreover, $(N-C)_{sub}$ bond formation shares a degree of charge separation, as supported by the change in Mulliken charges on going from the ground state to **TS-2S** [Mulliken charges: N_{sub} (−0.695), C_{sub1} (−0.387) for **11a**; N_{sub} (−0.670), C_{sub1} (−0.480) for **TS-2S**].

Interestingly, irrespective of whether the transition states **TS-2S** and **TS-2R** for the aliphatic substrate **3a** adopt a chairlike or

Table 1. Tetrahedral Twist Angles (θ_{TTA}), Selected NBO Donor−Acceptor Stabilization Energies (E_{NBO}), and Selected Bond Distances in TS-1S, TS-1R, TS-2S, and TS-2R

	E_{NBO} (kcal/mol) (bond distance (Å))			
transition state	$(C_{sub2}-C_{sub1})\rightarrow Cu$	$N_{sub}\rightarrow Cu$	$N_{sub}\rightarrow(C_{sub2}-C_{sub1})$	θ_{TTA}
TS-1S	12.13 (2.12)	11.28 (2.18)	30.84 (2.05)	26.25°
TS-1R	9.17 (2.16)	10.07 (2.08)	25.80 (2.08)	50.45°
TS-2S	10.45 (2.13)	11.15 (2.14)	25.70 (2.09)	13.38°
TS-2R	8.64 (2.17)	12.64 (2.09)	25.91 (2.10)	44.21°

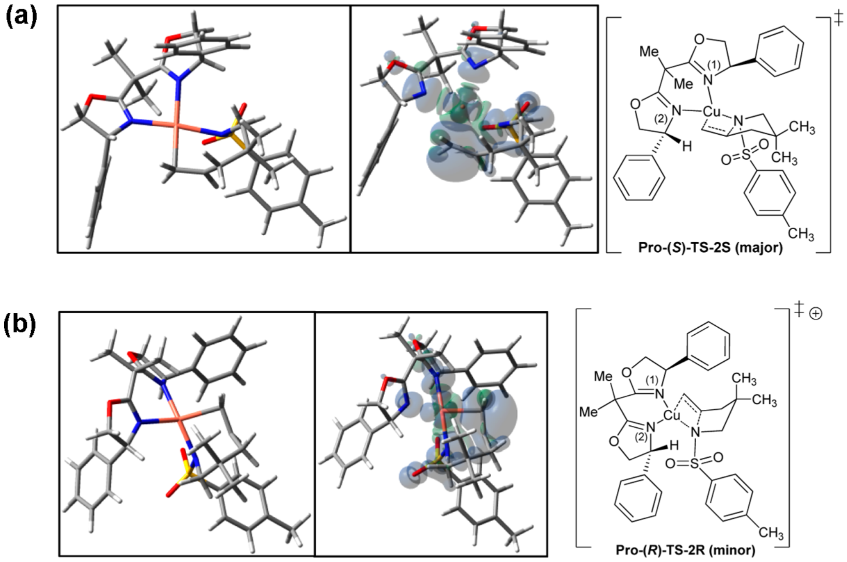

Figure 5. (a) Computed *N*-tosyl-2,2-dimethylpent-4-en-1-amine pro-(*S*) $(N-C)_{sub}$ bond-forming transition-state structure (**TS-2S**). Mulliken charges: $N_{lig(1)}$ (−0.467), $N_{lig(2)}$ (−0.468), Cu (0.392), N_{sub} (−0.670), C_{sub1} (−0.480), C_{sub2} (0.076), S (1.304). Spin densities: Cu (43.1%), N_{sub} (16.4%), C_{sub1} (24.7%), $N_{lig(1)}$ and $N_{lig(2)}$ (10%). (b) Computed *N*-tosyl-2,2-dimethylpent-4-en-1-amine pro-(*R*) $(N-C)_{sub}$ bond-forming transition-state structure (**TS-2R**). Mulliken charges: $N_{lig(1)}$ (−0.467), $N_{lig(2)}$ (−0.461), Cu (0.318), N_{sub} (−0.668), C_{sub1} (−0.448), C_{sub2} (0.046), S (1.307). Spin densities: Cu (39.9%), N_{sub} (17.6%), C_{sub1} (31.2%), $N_{lig(1)}$ and $N_{lig(2)}$ (7.6%).

a boatlike geometry, the $(N-C)_{sub}$ bond-forming distances and their respective NBO $N_{LP}\rightarrow\pi^*_{C=C}$ donor−acceptor energies remain similar (Table 1). On the other hand, the C_{sub1}−Cu bond is comparatively shorter in **TS-2S** and has a much greater donor−acceptor stabilization energy (Table 1). Consistent with the results for the previous substrate, these data suggest that **TS-2S** is more developed than **TS-2R**. Furthermore, the elongated N_{sub}−Cu bond distance in **TS-2S** compared with **TS-2R** (Table 1) is accompanied by a larger shift in charge density to the terminal alkene carbon (C_{sub1}), as evidenced by an increase in the computed Mulliken charges (Figure 5). As summarized in Table 1, both pro-(*S*) transition states have lower distortion from planarity (lower θ_{TTA}) than the corresponding pro-(*R*) transition states.

Further analysis of the interatomic distances in **TS-1S** and **TS-2S** (Table 1) reveals C_{sub1}−Cu bond-forming distances of 2.12 and 2.13 Å and $(N-C)_{sub}$ bond-forming distances of 2.05 and 2.09 Å, respectively. In comparison, the final C_{sub1}−Cu bond distances in the local minima **12** and **13** (Scheme 2; vide infra) were both found to be 1.98 Å, while the final $(N-C)_{sub}$ bond distances were 1.53 and 1.52 Å, respectively. Taken together, these results suggest that C_{sub1}−Cu bond formation is significantly more developed at the transition state than $(N-C)_{sub}$ bond formation, indicating that C_{sub1}−Cu bond formation precedes $(N-C)_{sub}$ bond formation in a concerted, asynchronous manner, consistent with previous results.[18]

Rationalization of Observed Selectivity Trends on the Basis of Substrate Structure. Experimentally, it is observed that smaller sulfonamide R groups on the substrate give lower levels of enantioselectivity in the reaction (eqs 1−5; vide supra). For example, aryl sulfonamides provide higher selectivity than methyl (e.g., Ts vs Ms), and even higher enantioselectivity is observed with substrates bearing the 3,5-di-*tert*-butylbenzenesulfonamide group (eqs 2 and 4). This is seen as a general trend for the synthesis of indolines and pyrrolidines via the copper-catalyzed aminooxygenation, aminohalogenation, and carboamination reactions (eqs 1−4). It is also observed experimentally that 4-pentenylsulfonamides with 2,2-*gem*-dialkyl or 2,2-*gem*-diaryl backbone substitution react with higher enantioselectivity than the parent 4-pentenylsulfonamides (eqs 3 and 4).

To discern the origin of these observations, the effects of N substitution on the selectivity were investigated by DFT. Having already considered the *N*-tosyl substrate, we turned our attention to an analysis of *N*-3,5-di-*tert*-butylbenzenesulfonamide **3b** and the *N*-mesyl substrate **3c**. Most importantly, the relative energetic preferences calculated for the pro-(*S*) transition states for substrates **3a**−**3c** were qualitatively consistent with the experimentally observed enantioselectivities [**3a** = 94% ee (2.7 kcal/mol), **3b** = 96% ee (3.0 kcal/mol), and **3c** = 86% ee (2.0 kcal/mol); eqs 2−4, vide supra]. The pro-(*S*) and pro-(*R*) transition states of **3b** (Figure 6) and **3c** (Figure 7) share a number of key features with those of **3a**. In particular, the calculated pro-(*S*) transition states (**TS-3S** and **TS-4S**) possess distorted square-planar geometries (Table 2) wherein the substrate backbones adopt chairlike conformations. Comparatively, the pro-(*R*) transition states (**TS-3R** and **TS-4R**) possess distorted tetrahedral geometries and adopt boatlike conformations. What is more, the computed interatomic distances and Mulliken charges (Tables 2 and 3) indicate that the pro-(*S*) transition states are more developed than the pro-(*R*) transition states. Specifically, the $(N-C)_{sub}$ and C_{sub1}−Cu bond-forming distances in **TS-3S** and **TS-4S** are slightly shorter than those in **TS-3R** and **TS-4R**, and the N_{sub}−Cu bond-breaking distances are noticeably longer. As well, the pro-(*S*) transition states display larger Mulliken charges on copper and the internal olefinic carbon. In terms of the observed differences in enantioselectivity, the increased preferences for the pro-(*S*) transition states over the pro-(*R*) transition states in the cases of **3a** and **3b** are attributed to the greater ability of the pro-(*S*) transition states to accommodate steric bulk on R^1 on account of the quadrant model. Additionally, the pro-(*S*) transition states are further stabilized by the presence of a C−H···π interaction between the substrate's R^2 methyl group and its R^1 aryl group (R groups refer to eq 2). The existence of this interaction was supported by an atoms in molecules (AIM)

Scheme 2. Proposed Copper-Catalyzed Aminooxygenation Reaction Coordinates: Path A Is for *N*-Tosyl-2,2-dimethylpentenamine (3a), and Path B Is for *N*-Tosyl-*o*-allyl Aniline (1a)

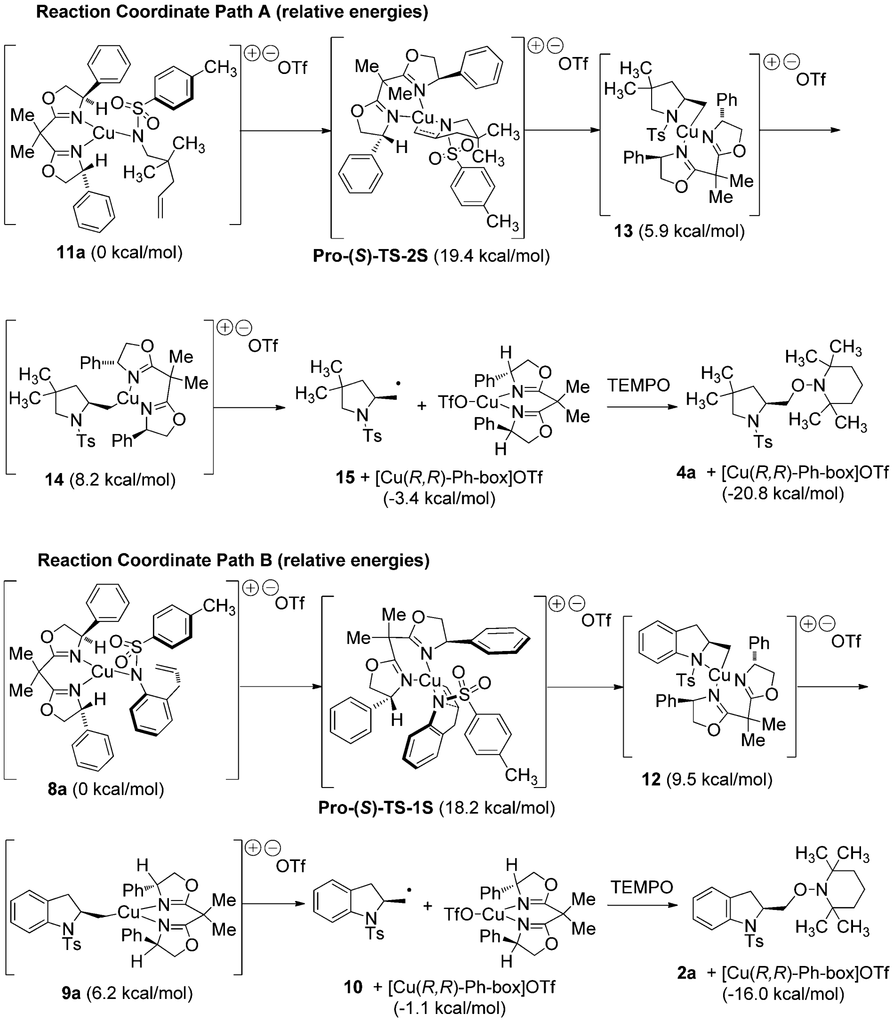

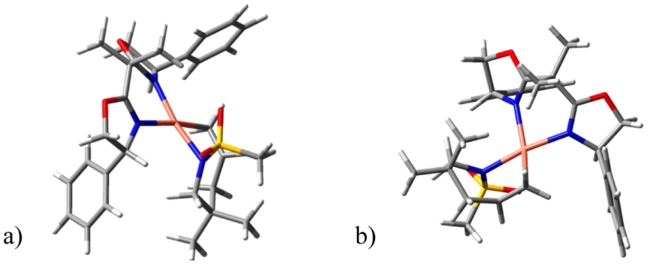

Figure 6. Computed *N*-mesyl-2,2-dimethylpent-4-en-1-amine (**3c**) transition-state structures: (a) pro-(*S*) **TS-3S** (major, chairlike); (b) pro-(*R*) **TS-3R** (minor, boatlike).

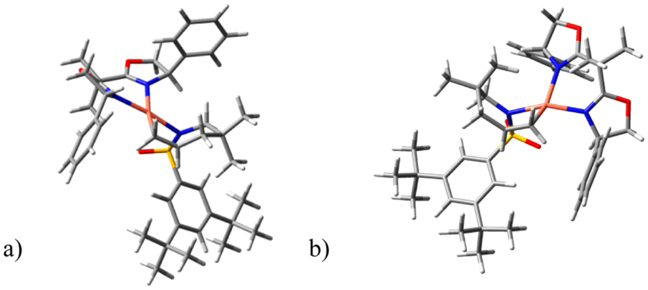

Figure 7. (a) Computed *N*-3,5-di-*tert*-butylbenzenesulfonamide (**3b**) transition-state structures: pro-(*S*) **TS-4S** (major, chairlike); (b) pro-(*R*) **TS-4R** (minor, boatlike).

analysis, which revealed the presence of a bond critical point (BCP) between a hydrogen of the R^2 methyl group and the π-system of the R^1 aryl ring (see the Supporting Information). Moreover, when R^1 = Ms, not only is this stabilizing interaction not present, but it is instead replaced by a repulsive interaction, thus decreasing the energetic preference of **TS-4S** over **TS-4R**.

To investigate the effect of the geminal dimethyl group of the substrate on the reaction selectivity, the 3,5-di-*tert*-butylbenzenesulfonamide of pent-4-en-1-amine, **3e**, which lacks the geminal dimethyl group, was considered. Experimentally, substrates that lack geminal dialkyl or diaryl substitution (e.g., **3d** and **3e**) give about 10% lower enantioselectivity than substrates with geminal disubstitution (e.g., **3a** and **3b**) (eqs 3 and 4). The computed transition states for **3e** (Figure 8) also showed a lower level of selectivity compared with **3b** (computed ee = 93% vs 96%). The origin of this decrease in selectivity is attributed in part to a greater range of motion of the *N*-tosyl substituent, which in turn allows it to move away from the occupied quadrant, and a less favorable C–H···π interaction in the chair-type transition state of **3e** (**TS-5S**) compared with that of **3b** (**TS-4S**). In **TS-4S**, the distance

Table 2. **Tetrahedral Twist Angles (θ_{TTA}) and Selected Bond Distances in TS-3S, TS-3R, TS-4S, TS-4R, TS-5S, and TS-5R**

	bond distances (Å)			
transition state	$C_{sub1}-Cu$	$N_{sub}-Cu$	$(C-N)_{sub}$	θ_{TTA}
TS-3S	2.14	2.14	2.08	12.98°
TS-3R	2.17	2.09	2.10	23.22°
TS-4S	2.15	2.13	2.07	12.78°
TS-4R	2.08	2.08	2.08	42.33°
TS-5S	2.14	2.11	2.08	7.78°
TS-5R	2.18	2.07	2.10	51.4°

between the methyl C−H and the nearest carbon of the aryl ring is 2.77 Å, possessing a BCP ρ_b of 0.0068, while in **TS-5S** the distance between the methylene C−H and the nearest carbon of the aryl ring is 3.01 Å, and the BCP ρ_b is 0.0050.

With an understanding of the underlying factors governing the stereodetermining Cu-mediated C−N bond formation, our interest turned to the overall reaction pathway. The complete mechanisms for the enantioselective copper-catalyzed aminooxygenations of substrates **1a** and **3a** are shown in Scheme 2. The reaction coordinates for the aminooxygenation of *N*-tosyl-2,2-dimethylpentenamine **3a** (path A) and *N*-tosyl-*o*-allyl aniline **1a** (path B) are shown in Figure 9 (coordinates and thermochemical data for all of the calculated transition states and intermediates can be found in the Supporting Information).

The ground-state energies for paths A and B were both arbitrarily set to 0.0 kcal/mol in order to draw comparisons from their relative energetic trends. The rate-limiting aminocupration steps have activation free energies ($\Delta G^{\ddagger}$) of 19.4 kcal/mol for path A and 18.2 kcal/mol for path B. In practice, the *N*-tosyl-*o*-allyl aniline-derived substrate **1a** is more reactive than the 4-pentenylsulfonamide **3a**, in agreement with the calculated relative energies. The first calculated intermediates to emerge from the aminocupration step are the organocopper intermediates **12** and **13**, in which the sulfonamide nitrogens are still coordinated to the copper. Rotation about the resulting Cu−C bond eliminates the N···Cu coordination, providing **14** and **9a**, respectively. This step is slightly endothermic in path A and slightly exothermic in path B, perhaps reflecting the relative basicities of the two nitrogens. Intermediates **14** and **9a** are charge-separated tricoordinate copper(I) complexes with the triflate residing in the outer sphere. Covalent attachment of the triflate to the copper center resulted in higher-energy intermediates. Energetically favorable C−Cu homolysis then ensues, providing the primary alkyl radicals **15** and **10** and [Cu(*R*,*R*)-Ph-box]OTf, a Cu(I) species. The alkyl radicals are then trapped by TEMPO, providing the aminooxygenation products (path A, $\Delta G_{rxn} = -20.8$ kcal/mol; path B, $\Delta G_{rxn} = -16.0$ kcal/mol).

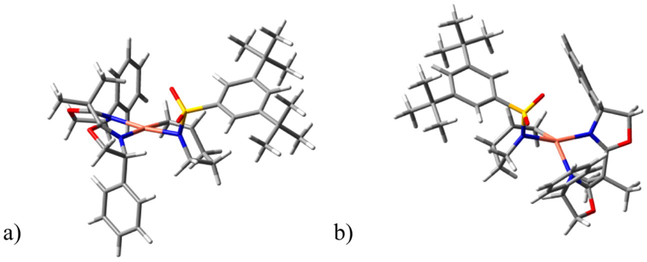

Figure 8. Computed *N*-(di-*tert*-butylphenylsulfonyl)-pent-4-en-1-amine (**3e**) transition-state structures: (a) pro-(*S*) **TS-5S** (major, chairlike); (b) pro-(*R*) **TS-5R** (minor, boatlike).

CONCLUSION

In summary, we have presented a rationale that accounts for the enantioselectivity of the [Cu(*R*,*R*)-Ph-box]$(OTf)_2$-catalyzed intramolecular aminooxygenation of γ-unsaturated sulfonamides using density functional theory. The stereochemical preference of the pro-(*S*) transition states involves the interplay between optimal orbital overlap, quadrant-based steric repulsion, and the tetrahedral twist angle (θ_{TTA}). In particular, we have found that for the substrates investigated herein, the favored pro-(*S*) transition states contain copper(II) centers with distorted square-planar geometries, while the minor pro-(*R*) transition states contain copper(II) centers with geometries more consistent with distorted tetrahedral coordination. The calculated bond lengths, E_{NBO} values, and Mulliken charges indicate that those transition states having square-planar copper(II) geometry are more developed as a result of better orbital overlap. In addition, a conformational trend for the pro-(*S*) and pro-(*R*) transition states of the examined *N*-(4-pentenyl)sulfonamides emerged: the major pro-(*S*) transition states adopt chairlike seven-membered cyclization conformations while the minor pro-(*R*) transition states adopt boatlike seven-membered cyclization conformations. Both the change in geometry about copper(II) and the change in cyclization conformation appear to be the result of minimization of steric interactions between the substrate's *N*-sulfonyl group and the phenyl substituent of the bis(oxazoline) ligand in the pro-(*R*) transitions states, as per the quadrant model. Thus, the substrate's *N*-sulfonyl group plays a significant role in the reaction's enantioselectivity, which was further observed by changes in selectivity with changes in the *N*-sulfonyl group. The

Table 3. **Selected Mulliken Charges in TS-3S, TS-3R, TS-4S, TS-4R, TS-5S, and TS-5R**

transition state	$N_{lig(1)}$	$N_{lig(2)}$	Cu	N_{sub}	C_{sub2}	C_{sub1}	S
TS-3S	−0.467	−0.474	0.394	−0.671	0.068	−0.483	1.295
TS-3R	−0.463	−0.465	0.353	−0.672	0.048	−0.548	1.288
TS-4S	−0.467	−0.459	0.379	−0.672	0.067	−0.480	1.316
TS-4R	−0.469	−0.464	0.316	−0.669	0.046	−0.449	1.319
TS-5S	−0.463	−0.466	0.417	−0.661	0.069	−0.478	1.303
TS-5R	−0.456	−0.473	0.382	−0.670	0.049	−0.456	1.306

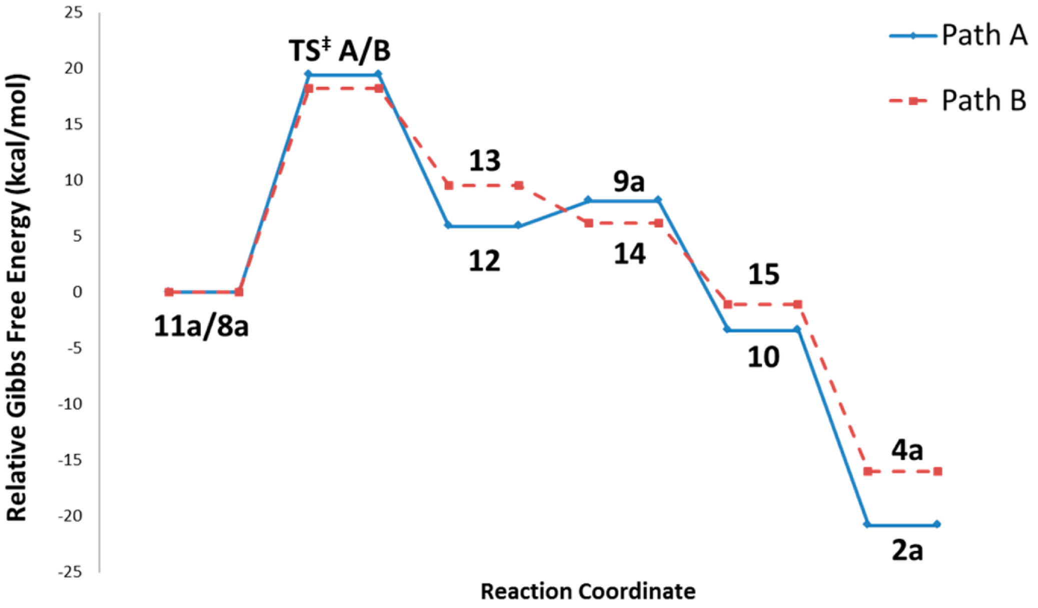

Figure 9. Calculated free energy profiles for the Cu(II)−bis(oxazoline)-catalyzed aminooxygenation of *N*-tosyl-2,2-dimethylpentenamine (substrate **3a**, path A) and *N*-tosyl-*o*-allyl aniline (substrate **1a**, path B).

pro-(*S*) and pro-(*R*) transition states described in this paper are similar to those proposed for other metal-catalyzed enantioselective *cis*-aminometalation/cyclization reactions (e.g., hydroamination with lanthanides)[41] in that a seven-membered chairlike conformation is invoked for the major transition state, but to our knowledge, this is the first time that a boatlike conformation has been invoked to rationalize product formation through the minor transition state. The sterically demanding sulfonamide moiety in our substrates makes alternative minor chairlike transition states more energetically demanding. The results described in this report should aid in the more complete understanding and further design of the growing body of alkene difunctionalization reactions catalyzed by [Cu(*R*,*R*)-Ph-box](OTf)$_2$ and related catalysts.[6−14]

■ ASSOCIATED CONTENT

Ⓢ Supporting Information

Relative energies for transition states **TS-1**, **TS-2**, **TS-3**, **TS-4**, and **TS-5** arising from single-point calculations; AIM data and calculated structures for **TS-4S** and **TS-5S**; and input parameters, thermochemical data, and coordinates of all computed structures. This material is available free of charge via the Internet at http://pubs.acs.org.

■ AUTHOR INFORMATION

Corresponding Author

*E-mail: tdudding@brocku.ca.

Notes

The authors declare no competing financial interest.

■ ACKNOWLEDGMENTS

Financial support for this work was provided by the National Institutes of Health NIGMS (GM-078383), and L.B. was the recipient of a Queen Elizabeth II Scholarship. We thank Dr. Yan Miller for helpful suggestions and SHARCNET (http://www.sharcnet.ca) for computing resources.

■ REFERENCES

(1) Chemler, S. R. *Org. Biomol. Chem* **2009**, *7*, 3009−3019.
(2) McDonald, R. I.; Liu, G.; Stahl, S. S. *Chem. Rev.* **2011**, *111*, 2981−3019.
(3) Zaitsev, A. B.; Adolfsson, H. *Synthesis* **2006**, 1725−1756.
(4) De Jong, S.; Nosal, D. G.; Wardrop, D. J. *Tetrahedron* **2012**, *68*, 4067−4105.
(5) Donohoe, T. J.; Callens, C. K. A.; Lacy, A. R.; Winter, C. *Eur. J. Org. Chem.* **2012**, 655−663.
(6) Zeng, W.; Chemler, S. R. *J. Am. Chem. Soc.* **2007**, *129*, 12948−12949.
(7) Fuller, P. H.; Kim, J.-W.; Chemler, S. R. *J. Am. Chem. Soc.* **2008**, *130*, 17638−17639.
(8) Sequiera, F. C.; Turnpenny, B. W.; Chemler, S. R. *Angew. Chem., Int. Ed.* **2010**, *49*, 6365−6368.
(9) Miao, L.; Haque, I.; Manzoni, M. R.; Tham, W. S.; Chemler, S. R. *Org. Lett.* **2010**, *12*, 4739−4741.
(10) Liwosz, T. W.; Chemler, S. R. *J. Am. Chem. Soc.* **2012**, *134*, 2020−2023.
(11) Bovino, M. T.; Chemler, S. R. *Angew. Chem., Int. Ed.* **2012**, *51*, 3923−3927.
(12) Miller, Y.; Miao, L.; Chemler, S. R. *J. Am. Chem. Soc.* **2012**, *134*, 12140−12156.
(13) Turnpenny, B. W.; Hyman, K. L.; Chemler, S. R. *Organometallics* **2012**, *31*, 7819−7822.
(14) Sanjaya, S.; Chiba, S. *Org. Lett.* **2012**, *14*, 5342−5345.
(15) Desimoni, G.; Faita, G.; Jørgensen, K. A. *Chem. Rev.* **2006**, *106*, 3561−3651.
(16) Johnson, J. S.; Evans, D. A. *Acc. Chem. Res.* **2000**, *33*, 325−335.
(17) Rasappan, R.; Laventine, D.; Reiser, O. *Coord. Chem. Rev.* **2008**, *252*, 702−714.
(18) Paderes, M. C.; Belding, L.; Fanovic, B.; Keister, J. B.; Dudding, T.; Chemler, S. R. *Chem.—Eur. J.* **2012**, *18*, 1711−1726.
(19) Paderes, M. C.; Chemler, S. R. *Org. Lett.* **2007**, *9*, 2745−2758.
(20) Paderes, M. C.; Chemler, S. R. *Eur. J. Org. Chem.* **2011**, 3679−3684.
(21) Paderes, M. C.; Keister, J. B.; Chemler, S. R. *J. Org. Chem.* **2013**, *78*, 506−515.
(22) Becke, A. D. *J. Chem. Phys.* **1993**, *98*, 5648−5652.
(23) Lee, C.; Yang, W.; Parr, R. G. *Phys. Rev. B* **1988**, *37*, 785−789.
(24) Frisch, M. J.; Trucks, G. W.; Schlegel, H. B.; Scuseria, G. E.; Robb, M. A.; Cheeseman, J. R.; Scalmani, G.; Barone, V.; Mennucci,

B.; Petersson, G. A.; Nakatsuji, H.; Caricato, M.; Li, X.; Hratchian, H. P.; Izmaylov, A. F.; Bloino, J.; Zheng, G.; Sonnenberg, J. L.; Hada, M.; Ehara, M.; Toyota, K.; Fukuda, R.; Hasegawa, J.; Ishida, M.; Nakajima, T.; Honda, Y.; Kitao, O.; Nakai, H.; Vreven, T.; Montgomery, J. A., Jr.; Peralta, J. E.; Ogliaro, F.; Bearpark, M.; Heyd, J. J.; Brothers, E.; Kudin, K. N.; Staroverov, V. N.; Kobayashi, R.; Normand, J.; Raghavachari, K.; Rendell, A.; Burant, J. C.; Iyengar, S. S.; Tomasi, J.; Cossi, M.; Rega, N.; Millam, J. M.; Klene, M.; Knox, J. E.; Cross, J. B.; Bakken, V.; Adamo, C.; Jaramillo, J.; Gomperts, R.; Stratmann, R. E.; Yazyev, O.; Austin, A. J.; Cammi, R.; Pomelli, C.; Ochterski, J. W.; Martin, R. L.; Morokuma, K.; Zakrzewski, V. G.; Voth, G. A.; Salvador, P.; Dannenberg, J. J.; Dapprich, S.; Daniels, A. D.; Farkas, Ö.; Foresman, J. B.; Ortiz, J. V.; Cioslowski, J.; Fox, D. J. *Gaussian 09*, revision C.01; Gaussian, Inc.: Wallingford, CT, 2009.

(25) Dunning, T. H., Jr.; Hay, P. J. In *Methods of Electronic Structure Theory*; Schaefer, H. F., III, Ed.; Modern Theoretical Chemistry, Vol. 3; Plenum: New York, 1977; pp 1−28.

(26) Hay, P. J.; Wadt, W. R. *J. Chem. Phys.* **1985**, *82*, 270−283.

(27) Hay, P. J.; Wadt, W. R. *J. Chem. Phys.* **1985**, *82*, 299−310.

(28) Wadt, W. R.; Hay, P. J. *J. Chem. Phys.* **1985**, *82*, 284−298.

(29) Tomasi, J.; Mennucci, B.; Cance, E. *J. Mol. Struct.: THEOCHEM* **1999**, *464*, 211−226.

(30) Although DCM has elsewhere been used to represent TFT because of its higher similarity in dielectric constant (see: Paton, R. S.; Goodman, J. M.; Pellegrinet, S. C. *Org. Lett.* **2009**, *11*, 37−40), DCE was deemed to have a solvent cavity size closer to that of TFT with a sufficiently similar dielectric constant.

(31) Fukui, K. *Acc. Chem. Res.* **1981**, *14*, 363−368.

(32) Chai, J. D.; Head-Gordon, M. *Phys. Chem. Chem. Phys.* **2008**, *10*, 6615−6620.

(33) Glendening, E. D.; Reed, A. E.; Carpenter, J. E.; Weinhold, F. *NBO*, version 3.1; University of Wisconsin: Madison, WI, 1990.

(34) Macrae, C. F.; Bruno, I. J.; Chisholm, J. A.; Edgington, P. R.; McCabe, P.; Pidcock, E.; Rodriguez-Monge, L.; Taylor, R.; van de Streek, J.; Wood, P. A. *J. Appl. Crystallogr.* **2008**, *41*, 466−470.

(35) Hehre, W. J. *Spartan '04*; Wavefunction, Inc.: Irvine, CA, 2003.

(36) Persson, I.; Persson, P.; Sandström, M.; Ullström, A.-S. *J. Chem. Soc., Dalton Trans.* **2002**, 1256−1265.

(37) Thorhauge, J.; Robertson, M.; Hazell, R. G.; Jorgensen, K. A. *Chem.—Eur. J.* **2002**, *8*, 1888−1898.

(38) Paschke, R.; Liebsch, S.; Tschierske, C.; Oakley, M. A.; Sinn, E. *Inorg. Chem.* **2003**, *42*, 8230−8240.

(39) Bocian, D. F.; Pickett, H. M.; Rounds, T. C.; Strauss, H. L. *J. Am. Chem. Soc.* **1975**, *97*, 687−695.

(40) Yeh, P. L.; Tai, C. K.; Shih, T. L.; Hsiao, H. L.; Wang, B. C. *J. Mol. Struct.* **2012**, *1018*, 64−71.

(41) Hong, S.; Tian, S.; Metz, M. V.; Marks, T. J. *J. Am. Chem. Soc.* **2003**, *125*, 14768−14783.